ACS APPLIED MATERIALS & INTERFACES

www.acsami.org

Research Article

Boosting Photocatalytic Nitrogen Fixation via Nanoarchitectonics Using Oxygen Vacancy Regulation in W-Doped Bi_2MoO_6 Nanosheets

Manisha Sharma, Ashish Kumar, Deepika Gill, Shilpi Jaiswal, Abhijit Patra,* Saswata Bhattacharya,* and Venkata Krishnan*

Cite This: https://doi.org/10.1021/acsami.3c12563

Read Online

ACCESS | Metrics & More | Article Recommendations | Supporting Information

ABSTRACT: Ammonia and nitrates are key raw materials for various chemical and pharmaceutical industries. The conventional methods like Haber–Bosch and Ostwald methods used in the synthesis of ammonia and nitrates, respectively, result in harmful emission of gases. In recent years, the photocatalytic fixation of N_2 into NH_3 and nitrates has become a hot topic since it is a green and cost-effective approach. However, the simultaneous production of ammonia and nitrates has not been studied much. In this regard, we have synthesized W-doped Bi_2MoO_6 nanosheets in various molar ratios and demonstrated their potential as efficient photocatalysts for the simultaneous production of NH_3 and NO_3^- ions under visible light irradiation. It was found that one of the catalysts (BMWO0.4) having an optimal molar ratio of doped tungsten showed the best photocatalytic NH_3 production (56 μmol h^{-1}) without using any sacrificial agents along with the simultaneous production of NO_3^- ions at a rate of 7 μmol h^{-1}. The enhanced photocatalytic activity of the synthesized photocatalysts could be ascribed to oxygen vacancy defects caused by Mo substitution by a more electronegative W atom. Furthermore, density functional theory calculations verified the alteration in the band gap after doping of W atoms and also showed a strong chemisorption of N_2 over the photocatalyst surface leading to its activation and thereby enhancing the photocatalytic activity. Thus, the present work provides insights into the effect of structural distortions on tailoring the efficiency of materials used in photocatalytic N_2 fixation.

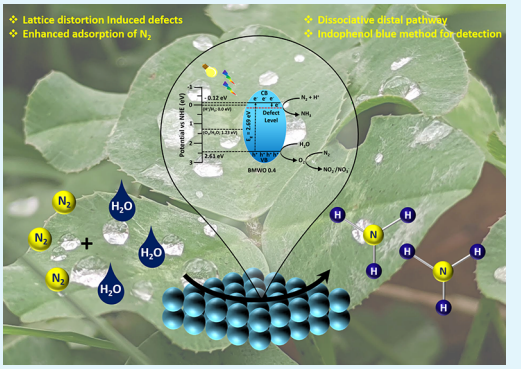

KEYWORDS: *photocatalysis, nitrogen fixation, Bi_2MoO_6, W-doping, oxygen vacancy, lattice distortion*

1. INTRODUCTION

The essential role of N_2 in the sustaining life on earth is well-known. However, due to its inert nature, most organisms cannot utilize N_2 directly. It is used either in its oxidized form as NO_3^- or in its reduced form as NH_3. Therefore, it is important to fix N_2 in the less inert or more reactive form to utilize it for various purposes. The fixation of N_2 occurs in either natural or industrial ways. In nature, the conversion of N_2 into NH_3 and NO_3^- happens via the nitrogenase enzyme and geothermal processes like lightning. In particular, NH_3 and nitrates are important industrial chemicals used to prepare fertilizers, pharmaceuticals, and other vital N-based chemicals.[1,2] The current global demand for NH_3 reaches around 150 million tons annually.[3] It is also regarded as a potential carrier of hydrogen as it contains 17.6 wt % hydrogen.[4,5] Thus, the demand for NH_3 is increasing day by day with increasing population and energy demands. The industrial way of fixing nitrogen is the Haber–Bosch process and Ostwald process for the generation of NH_3 and HNO_3, which is not green and sustainable because of their high energy demand and release of CO_2 into the atmosphere during the reaction process.[6] In the process of NH_3 production, 3–5% of natural gas and 1–3% of the world's electricity are being consumed and also lead to 1.2% of global CO_2 emissions.[7−9] Therefore, this is a high time to develop techniques that are green, efficient, sustainable, and more economical in comparison to this process.

The generation of NH_3 by photocatalytic nitrogen fixation is a fascinating alternative to the consumption of fossil fuel energy and subsequent CO_2 emissions involved in the Haber–Bosch process.[10] Photocatalysis is relatively cheap and provides a simple reaction system to produce NH_3 from N_2 and H_2O without polluting the environment.[11] In this process, the photoexcited electrons from a catalyst are transferred to the antibonding orbital of adsorbed N_2 molecules, resulting in their activation and further dissociation of the triple bond between N atoms.[3,12] The H atoms come directly from H_2O for the reduction of activated N_2 and hence eliminate the large

Received: August 23, 2023
Revised: October 30, 2023
Accepted: November 8, 2023

requirement of energy input as required in the Haber−Bosch process.[4] However, photocatalytic nitrogen fixation currently suffers from low efficiency because of the meager adsorption of N_2 over the surface of the photocatalyst and less utilization of incident light energy by the photocatalyst.[13] To increase the adsorption of N_2 over the surface of the photocatalyst, defect engineering is a promising technique that provides abundant active sites and decreases the activation energy for the reaction.[14] These defects can significantly increase the chemisorption of N_2 molecules and can also act as channels for electron transfer.[15] Numerous strategies have been developed to engineer various kinds of defects over the catalyst surface, such as vacancies (O, N, and S), ion doping, facet engineering, etc. Such type of nanoarchitectonics based materials are important in various catalytic processes.[16] Yuan et al. have reported the oxygen vacancies over a rutile TiO_2 surface using different calcinating temperatures. It was found that the NH_3 production was 6.5 times higher on oxygen vacancy-rich TiO_2 compared to the pristine TiO_2 using methanol as a hole scavenger.[3] Li et al. have reported the formation of oxygen vacancies over the surface of Bi_2MoO_6 using NaOH at room temperature.[11] Dong et al. have recently reported better nitrogen fixation using sulfur vacancy-rich Bi_2S_3 under solar light irradiation.[17] All of these reports suggest the influence of defects/vacancies in boosting the formation of NH_3 by increasing the catalytic sites significantly. Recently, another work on doping of Bi_2MoO_6 with In was reported for overall nitrogen fixation.[18] The amount of NH_3 and NO_3^- ions for In-doped Bi_2MoO_6 was found to be 53.4 and 54 μmol g^{-1} h^{-1}, respectively. However, there are fewer reports on simultaneous production of NH_3 and NO_3^- in a sustainable way. Also, there is still a need to investigate in detail more catalytic systems containing defects and the processes involved in photocatalytic nitrogen fixation to achieve better efficiency.

In recent years, layered perovskite oxides have attracted tremendous attention from researchers due to their sheet-like morphology and tunable structure.[19] Bi_2MoO_6 is a layered perovskite oxide having an Aurivillius phase with a visible light active bandgap. In the Aurivillius phase, $(MoO_4)^{2-}$ layers are interconnected with fluorite-like $(Bi_2O_2)^{2+}$ layers, having weak electrostatic interactions. The distorted geometry of $(MoO_4)^{2-}$ layers is prominently accountable for the photocatalytic activity of this material.[20] Nanoarchitectonics of oxygen vacancy-rich Bi_2MoO_6 has been investigated for many photocatalytic applications like removal of pollutants from wastewater, CO_2 reduction, and N_2 fixation because of its promising potential.[13,21,22] In addition, doping of Bi_2MoO_6 with various other elements like Fe, F, etc. and heterojunctions based Bi_2MoO_6 photocatalytic systems have also been explored for various applications.[23−25] However, there are no reports on W-doped Bi_2MoO_6 for photocatalytic nitrogen fixation to the best of our knowledge. The substitution of Mo with W can induce changes in the crystal structure and morphology because of the different atomic radii of Mo and W. These modifications in the crystal structure can change the optical response of the W-doped Bi_2MoO_6 and, hence, can amplify the photocatalytic activity.

Hence, in the present work, we have prepared W-doped Bi_2MoO_6 nanosheets via a facile hydrothermal method, wherein W has been used in different molar ratios (0.1, 0.2, 0.3, 0.4, 0.5, 0.7, 1.0). The W-doped Bi_2MoO_6 nanosheets have been characterized by various state-of-the-art techniques to explore the structure, morphology, and other salient properties. Subsequently, these nanosheets were employed for photocatalytic nitrogen fixation under visible light irradiation. Furthermore, temperature-programmed desorption (TPD) studies were performed to investigate the chemisorption of N_2 over catalytic sites and nitrogen fixation studies were also done using $^{15}N_2$ gas to unequivocally prove the source of nitrogen for NH_3 formation. The activity of the various W-doped Bi_2MoO_6 nanosheets was compared with pristine Bi_2MoO_6 and Bi_2WO_6 nanosheets to illustrate the efficiency of the doped catalysts. Specifically, this work sheds light on a facile technique to synthesize defect-rich photocatalysts by regulating both the nanostructure and band gap by simply adjusting the compositions of solutions and how the defects induced by doping contribute to the enhancement of photocatalytic activity toward nitrogen fixation.

2. EXPERIMENTAL DETAILS

2.1. Chemicals. Bismuth nitrate pentahydrate ($Bi(NO_3)_3{\cdot}5H_2O$) ≥ 98%, ammonium molybdate tetrahydrate ($(NH_4)_6Mo_7O_{24}{\cdot}H_2O$) ≥ 99%, sodium tungstate dihydrate ($Na_2WO_4{\cdot}2H_2O$) ≥ 99%, and ammonium chloride (NH_4Cl) ≥ 99% were obtained from Sigma-Aldrich, India. Trisodium citrate ($Na_3C_6H_5O_7$) was purchased from CDH Chemicals, India. Sodium nitroprusside ($C_5H_4FeN_6Na_2O_3$) was purchased from Loba Chemicals, India. Salicylic acid ($C_7H_6O_3$), sodium hydroxide (NaOH), *para*-dimethylamino benzaldehyde ($C_9H_{11}NO$), and concentrated HNO_3 were purchased from Merck, India. Sodium nitrate ($NaNO_3$) and sodium nitrite ($NaNO_2$) were purchased from Loba Chemicals, India. Sulfanilamide and *N*-(1-naphthyl) ethylenediamine dihydrocholoride were purchased from AR grade, India and SRL Chemicals, India. Deionized (DI) water was used from an ELGA PURELAB Option-R7 double-stage water purifier. Sodium potassium tartrate ($C_4H_4O_6KNa{\cdot}4H_2O$) was purchased from Sigma-Aldrich, India. $^{14}N_2$ ≥ 99% gas was purchased from Chandigarh Gases Pvt. Ltd., India, and $^{15}N_2$ ≥ 99% gas was purchased from Sigma-Aldrich, India.

2.2. Synthesis of Catalysts. *2.2.1. Synthesis of Bismuth Molybdate Nanosheets.* The synthesis of Bi_2MoO_6 nanosheets was performed by a facile hydrothermal method. In brief, 2 mmol (0.97 g) of bismuth nitrate ($Bi(NO_3)_3{\cdot}5H_2O$) was dissolved in 20 mL of nitric acid solution (2 mol L^{-1}). After stirring for 30 min, 10 mL of solution of 0.1 mol L^{-1} ammonium molybdate tetrahydrate ($(NH_4)_6Mo_7O_{24}{\cdot}4H_2O$) was added dropwise with continuous stirring. The stirring was maintained for another 30 min while the solution pH was fixed to 7 using ammonia solution. Finally, the precursor was transferred to a 50 mL Teflon-lined stainless-steel autoclave and was eventually heated at 180 °C for 24 h. Afterward, the autoclave was cooled to room temperature to collect the dark green precipitates of Bi_2MoO_6. The obtained product was washed numerous times with DI water and ethanol to discard any remaining impurities. At last, the obtained product was dried at 70 °C overnight in an oven and weighed 580 mg in yield.

2.2.2. Synthesis of Bismuth Tungstate Nanosheets. The Bi_2WO_6 nanosheets were prepared by a facile hydrothermal method. In brief, 2 mmol (0.97 g) of bismuth nitrate ($Bi(NO_3)_3{\cdot}5H_2O$) was dissolved in 20 mL of nitric acid solution (2 mol L^{-1}). After stirring for 30 min, 10 mL solution of 0.1 mol L^{-1} sodium tungstate dihydrate ($Na_2WO_4{\cdot}2H_2O$) was added dropwise while stirring was continuously maintained. The stirring was maintained for another 30 min while the solution pH was fixed to 7 using ammonia solution. Finally, the precursor was transferred to a 50 mL Teflon-lined stainless-steel autoclave and was eventually heated at 180 °C for 24 h. Afterward, the autoclave was cooled to room temperature to collect the dark green precipitates of Bi_2MoO_6. The obtained product was washed numerous times with DI water and ethanol to discard any remaining impurities. At last, the product was dried at 80 °C overnight in an oven and weighed 650 mg in yield.

2.2.3. Synthesis of Tungsten-Doped Bismuth Molybdate Nanosheets. The synthesis of W-doped Bi_2MoO_6 nanosheets was done by

https://doi.org/10.1021/acsami.3c12563
ACS Appl. Mater. Interfaces XXXX, XXX, XXX−XXX

Scheme 1. Schematic Illustration Depicting the Synthesis Procedure of W-Doped Bi_2MoO_6

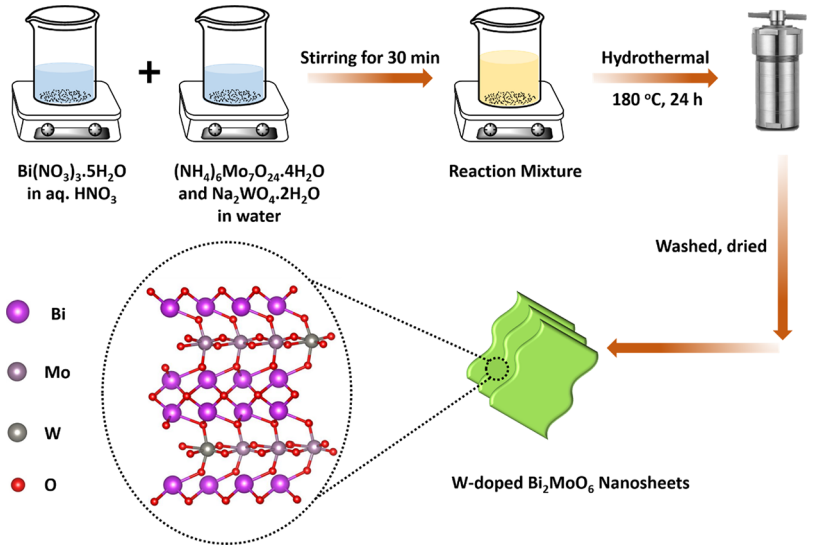

a facile hydrothermal method. In brief, 2 mmol (0.97 g) of bismuth nitrate ($Bi(NO_3)_3{\cdot}5H_2O$) was dissolved in 20 mL of nitric acid solution (2 mol L^{-1}). After stirring for 30 min, 10 mL solution of ammonium molybdate tetrahydrate ($(NH_4)_6Mo_7O_{24}{\cdot}4H_2O$) and sodium tungstate dihydrate ($Na_2WO_4{\cdot}2H_2O$) was added dropwise according to their molar ratios while stirring was continuously maintained. The stirring was maintained for another 30 min while the solution pH was fixed to 7 using ammonia solution. Finally, the precursor was transferred to a 50 mL Teflon-lined stainless-steel autoclave and was eventually heated at 180 °C for 24 h. Subsequently, the autoclave was cooled to room temperature to collect the green-colored precipitates to yellow-colored precipitates using a different molar ratio of W. The product was washed numerous times with DI water and ethanol to discard any remaining impurities. At last, the obtained product was dried at 80 °C overnight in an oven and named BMWO0.1, BMWO0.2, BMWO0.3, BMWO0.4, BMWO0.5, and BMWO0.7 depending upon the molar ratio of W used in the sample. The products weighed between 600 and 640 mg after drying.

2.3. Photocatalytic Nitrogen Fixation. Photocatalytic N_2 fixation experiments were conducted under closed conditions in a 100 mL round-bottom flask under visible light irradiation using an in-house built photoreactor having two 45 W white LED bulbs (intensity of light = 30,100 lx). In a typical reaction, 25 mg of the photocatalyst was dispersed ultrasonically in 50 mL of ultrapure deionized water. Subsequently, high-purity N_2 gas was purged into the reaction mixture at a rate of 40 mL min^{-1} for 45 min under constant stirring. Finally, the reaction was started by irradiating visible light for 2 h. Then, 2 mL samples were collected after a fixed time interval (30 min) with the help of a syringe. The collected samples were centrifuged at 12,000 rpm to remove the solid catalyst powder. For the quantification of generated NH_3, an improved indophenol method was used where salicylic acid was used instead of phenol, as reported in the literature.[26] In this method, NH_4^+ ions react with salicylic acid and sodium hypochlorite to form a blue compound called indophenol. In short, 2 mL of solution collected earlier from the reaction mixture was centrifuged to remove the catalyst. Then, 1 mL of 1 M NaOH containing 0.5 M salicylic acid and 0.2 M trisodium citrate was added followed by the 50 μL addition of sodium hypochlorite. Subsequently, 0.2 mL of 0.025 M solution of sodium nitroferricyanide dihydrate was added. The solution was mixed and left to develop the color. After complete coloration (40−45 min), the concentration of NH_3 formed was estimated by monitoring and comparing the absorption at 655 nm against the absorption of standard NH_4Cl aqueous solutions of different molarities. The remaining 1 mL of the solution collected from the reaction mixture earlier was subjected to the Watt−Chrisp method to quantify the formation of hydrazine (N_2H_4).[27] In brief, 2 g of para(dimethylamino)benzaldehyde with 10 mL of concentrated HCl and 100 mL of ethanol was mixed together and used as a reagent for the determination of hydrazine. Then, 1 mL of this reagent mixture was added to the remaining 1 mL of the reaction mixture. After 30 min, the absorption of the solution was measured at 455 nm using a UV−vis spectrometer. In addition, the formation of other oxidized products like nitrate (NO_3^-) and nitrite ions (NO_2^-) was detected using UV−vis spectroscopic method. The detection method for these ions is described in the Supporting Information section. The absorption of standard solutions for NO_3^- and NO_2^- ions was measured at 220 and 540 nm, respectively.

To ensure that NH_3 has been formed from purged N_2 gas, photocatalytic experiments with $^{15}N_2$ gas were performed under similar conditions. For the detection of the formed products, the same improved indophenol method and Watt−Chrisp method were used. In addition, mass spectrometric analyses were also performed to obtain deeper insights into the nitrogen source used for ammonia formation. After completion of the reaction, the remaining reaction mixture was subjected to nuclear magnetic resonance (NMR) studies. 40 mL of the reaction mixture was taken out and centrifuged. 2 M H_2SO_4 was added to the reaction mixture until the pH was equal to 2. Then, the solution was evaporated using a rotary evaporator until 1 mL of the mixture remained. 500 μL of the remaining mixture and 600 μL of DMSO-d_6 were mixed together. Afterward, 700 μL solution was taken out and NMR spectra was recorded. Also, the turnover frequency (TOF) was calculated for the photocatalytic nitrogen fixation using the following formula:[28]

$$\mathrm{TOF} = \frac{\mathrm{Numberofmoles of NH_3 generated per hour}}{\mathrm{Numberofactive sites}}$$

3. RESULTS AND DISCUSSION

3.1. Synthesis, Structural, and Optical Studies. The synthesis of W-doped Bi_2MoO_6 nanosheets was performed by using a facile hydrothermal method as shown in Scheme 1. First, powder X-ray diffraction (XRD) patterns for all the samples (Bi_2MoO_6, BMWO0.1, BMWO0.2, BMWO0.3, BMWO0.4, BMWO0.5, BMWO0.7, and Bi_2WO_6) were recorded. The diffraction patterns of Bi_2MoO_6 and Bi_2WO_6 were found to be similar to the JCPDS card no. 72-1574, (a = 5.506 Å, b = 16.2260 Å, c = 5.487 Å) and JCPDS Card no. 39-0256, (a = 5.456 Å, b = 16.445 Å, c = 5.444 Å), respectively.[29] The diffraction patterns of all W-doped Bi_2MoO_6 samples were found to be similar to those of Bi_2MoO_6 and Bi_2WO_6. The

https://doi.org/10.1021/acsami.3c12563
ACS Appl. Mater. Interfaces XXXX, XXX, XXX−XXX

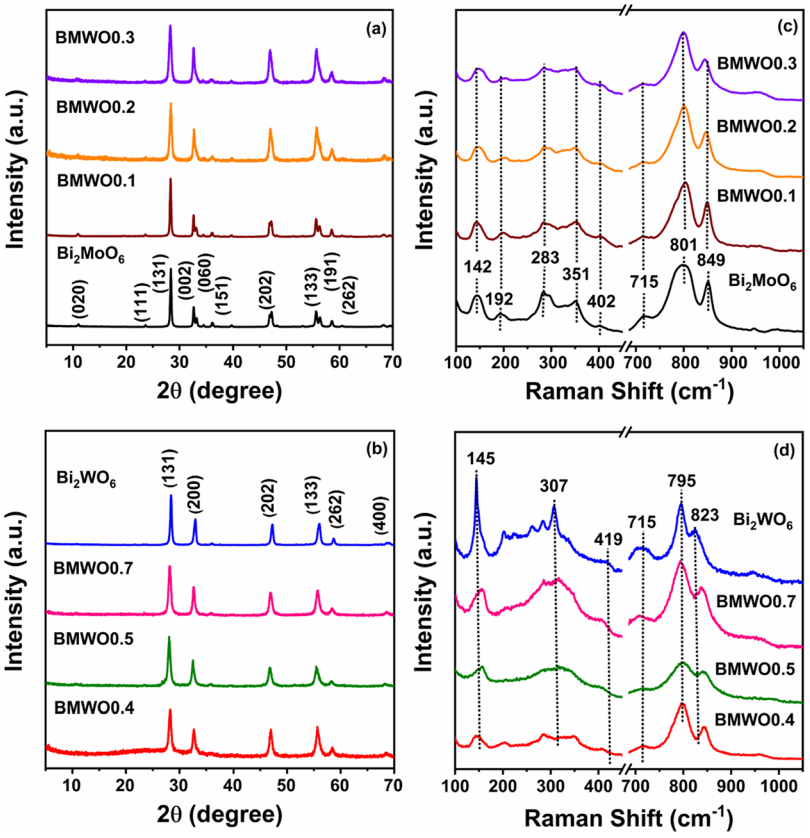

Figure 1. (a, b) PXRD patterns and (c, d) Raman spectra of Bi_2MoO_6, BMWO0.1, BMWO0.2, BMWO0.3, BMWO0.4, BMWO0.5, BMWO0.7, and Bi_2WO_6.

intensity of the peaks indicated the different concentrations of W in each sample (Figure 1a,b). The highest intensity peak for pristine Bi_2MoO_6 was observed at $2\theta = 28.37°$ corresponding to the (131) crystal plane, whereas the same peak was observed at $2\theta = 28.41°$ for pristine Bi_2WO_6. According to the literature, an increase in radius will increase the interplanar spacing (d) which will shift 2θ to smaller angles.[30] However, the effect of atomic radius on Bragg's equation ($2d \sin \theta = n\lambda$) is negligible. However, there is a significant effect of electronegativity on the shifting of angles. The electronegativity of W (2.36) is more than Mo (2.16), because of which W will form more covalent bonds and will shrink the Bi_2WO_6 crystal structure.[31] Hence, the interplanar distance (d) will be lesser in Bi_2WO_6 as compared to Bi_2MoO_6 and 2θ will shift to higher angles.[31] Also, it can be seen in PXRD plots that peak broadening is taking place from Bi_2MoO_6 to Bi_2WO_6. This broadening of PXRD patterns indicates the decrease in crystallinity of the samples, which is further proved by calculating the crystallite size using the Debye–Scherrer equation.[26] The calculated crystallite size and lattice strain of all of the samples corresponding to the highest intensity peak (131) has been provided in Table S1. Also, the lattice parameters calculated for W-doped Bi_2MoO_6 are presented in Table S2, which indicates distortion in the lattice structure with W doping.

In addition, Raman spectra of as-synthesized samples were also recorded and are presented in Figure 1c,d. The spectra have two main regions. The region below 400 cm^{-1} is assigned to the bending modes of the Mo–O/W–O bonds. Also, the possible stretching of Bi–O bonds comes under 400 cm^{-1}.[32] The region from 600 to 1000 cm^{-1} involves the stretching modes of MoO_6/WO_6 octahedra. This region provides insightful information about the stretching vibrational modes of MoO_6/WO_6 octahedra. The peaks at 801 and 845 cm^{-1} correspond to the antisymmetric and symmetric stretching modes (A_g) of the MoO_6 octahedra. It is observed that an increase in the concentration of W in the Bi_2MoO_6 crystal structure shifts the peaks at 801 and 845 cm^{-1} to lower wavenumbers. Eventually, these peaks for Bi_2WO_6 are observed at 795 and 823 cm^{-1}. These peak shifts indicate the successful substitution of Mo atoms from W atoms.[31]

Furthermore, Fourier transform infrared (FTIR) spectra of Bi_2MoO_6, BMWO0.4, and Bi_2WO_6 were recorded in the 400–4000 cm^{-1} range (Figure S1). The peaks between 570 and 600 cm^{-1} correspond to the bending modes of MoO_6 octahedra. A small peak at 797 and 844 cm^{-1} corresponds to asymmetric and symmetric stretching modes of apical oxygen atoms in MoO_6 octahedra.[33,34] The peak at 734 cm^{-1} corresponds to the asymmetric stretching mode of the Mo–O bond in MoO_6 octahedra. The oxygens atoms involved in this stretching mode are at the equatorial position.[35] The peak corresponding to the symmetric stretching of apical oxygen atoms has shifted to 840 cm^{-1} which indicates the successful incorporation of W in the Bi_2MoO_6 structure. Also, the peak related to the symmetric stretching mode of equatorial oxygen atoms in MoO_6 octahedra has shifted to a lower wavenumber at 725 cm^{-1}. The peaks for Bi_2WO_6 were observed at 820 cm^{-1} for the symmetric stretching of apical oxygen atoms and at 725 cm^{-1} for the symmetric stretching of equatorial oxygen atoms. The peaks at 1562, 1622, and 1617 cm^{-1} were observed for Bi_2MoO_6, BMWO0.4, and Bi_2WO_6, respectively corresponding to the O–H stretching of adsorbed water.[36,37] No peak was found between 450 and 650 cm^{-1}.

https://doi.org/10.1021/acsami.3c12563
ACS Appl. Mater. Interfaces XXXX, XXX, XXX–XXX

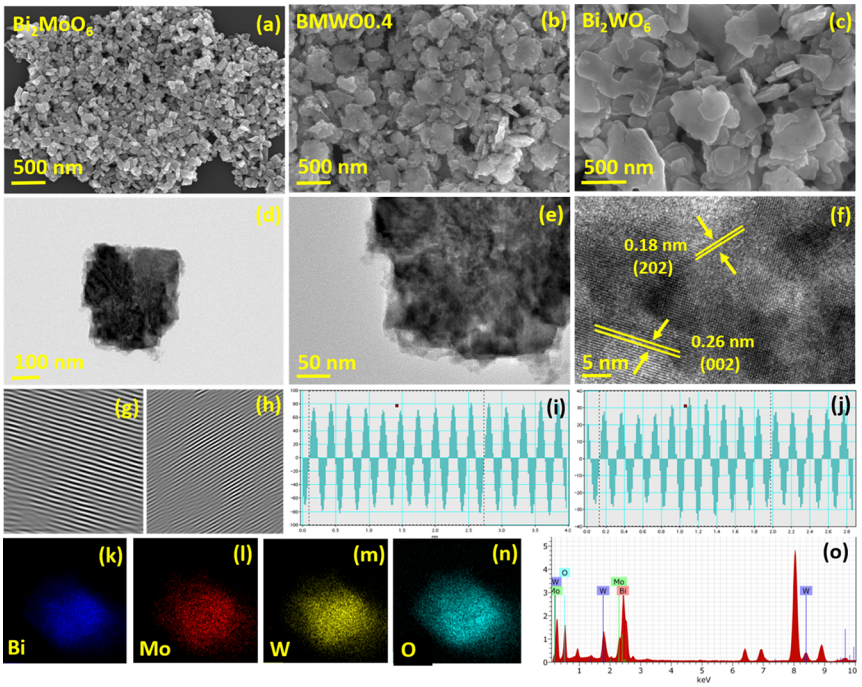

Figure 2. SEM images of (a) Bi_2MoO_6, (b) BMWO0.4, and (c) Bi_2WO_6; (d, e) TEM and (f) HRTEM images, (g, h) IFFT, (i, j) line analysis, (k–n) elemental mapping, and (o) EDAX spectra of BMWO0.4.

The effect of W-doping on the optical properties of Bi_2MoO_6 was also studied. After the incorporation of W in the Bi_2MoO_6 structure, a color change was observed (Figure S2). The dark green color of Bi_2MoO_6 was changed to light green for BMWO0.4 and to pale yellow for Bi_2WO_6. The obvious color change indicates the incorporation of W in the crystal structure of Bi_2MoO_6. Furthermore, the absorption and change in band gap were studied by UV–vis diffuse reflectance spectroscopy (DRS). There was a decrease in the band gaps of the samples from Bi_2MoO_6 to BMWO0.4 and then it started increasing from BMWO0.5 to Bi_2WO_6. The absorption spectra were red-shifted for the W-doped samples but not linearly. This could be because of two reasons. The first reason is the extent of involvement of Mo 4d orbitals and W 5d orbitals in the conduction band of the W-doped Bi_2MoO_6 samples. The conduction band of W-doped Bi_2MoO_6 comprises Mo 4d, W 5d, O 2p, and Bi 6p orbitals. The band gaps of W-doped Bi_2MoO_6 nanosheets have changed after using different molar ratios of Mo and W-precursors. Therefore, it can be evidenced that the composition of elements is capable of regulating the absorption of light.[31] Another reason is the degree of delocalization of excitation energy in the distorted crystal structure after the incorporation of W in the samples.[30] The band gap for Bi_2MoO_6, BMWO0.1, BMWO0.2, BMWO0.3, BMWO0.4, BMWO0.5, BMWO0.7, and Bi_2WO_6 was calculated to be 2.56, 2.53, 2.51, 2.46, 2.45, 2.48, 2.66, and 2.75 eV, respectively (Figure S3). Similar results have been reported earlier for Mo substitution in Bi_2WO_6.[30,38]

In addition, reflection electron energy loss spectroscopy (REELS) and ultraviolet photoelectron spectroscopy (UPS) studies were employed to further verify the band gap and valence band (VB) positions of Bi_2MoO_6, BMWO0.4, and Bi_2WO_6, respectively (Figure S4). The band gap of Bi_2MoO_6, BMWO0.4, and Bi_2WO_6 were determined to be 2.71, 2.69, and 2.83 eV, respectively which are close to those values calculated earlier using DRS method. Also, VB positions were calculated to be 2.45, 2.57, and 2.77 eV, respectively. Finally, the conduction band (CB) was calculated using the following equation.[39]

$$E_{CB} = E_{VB} - E_g$$

This comes out to be −0.26, −0.12, and −0.06 eV for Bi_2MoO_6, BMWO0.4, and Bi_2WO_6, respectively. The illustration of VB and CB of these samples has been shown in Figure S5.

3.2. Morphological and Compositional Studies. The morphological investigations on the as-prepared samples were performed by using scanning electron microscopy (SEM) and transmission electron microscopy (TEM). As shown in Figure 2a, the morphology of Bi_2MoO_6 was found to be plate-like, whereas Bi_2WO_6 showed a thin sheet-like shape (Figure 2c). For BMWO0.4, it can be seen in Figure 2b that with the incorporation of W in Bi_2MoO_6 there is a change in the morphology. The edges as well as surface of the sheets seem more distorted, indicating a slight change in morphology than the pristine counterparts. The TEM images of BMWO0.4 are shown in Figure 2d,e. TEM images of Bi_2MoO_6 and Bi_2WO_6 are presented in Figure S6a,b,g,h, respectively. Furthermore, HRTEM images of Bi_2MoO_6, BMWO0.4, and Bi_2WO_6 depict more structural features of the samples. The *d*-spacing for Bi_2MoO_6 (Figure S6c) and Bi_2WO_6 (Figure S6i) were determined to be 0.26 nm for both the samples correspond to the (002) lattice plane. The inverse fast Fourier transform (IFFT) and line profiles are shown in Figure S6d,e,j,k, respectively. Similarly, *d*-spacing for BMWO0.4 was found to be 0.26 and 0.18 nm corresponding to (002) and (202) lattice planes (Figure 2f).[40−42] Furthermore, the IFFT and line profile analyses of these lattice planes are shown in Figure 2g–j. The yellow highlighted part in IFFT images shows the disturbance in lattice planes because of W-doping in the Bi_2MoO_6 nanosheets. The elemental mapping and energy dispersive analysis (EDAX) spectra confirm the presence of Bi, Mo, W,

https://doi.org/10.1021/acsami.3c12563
ACS Appl. Mater. Interfaces XXXX, XXX, XXX−XXX

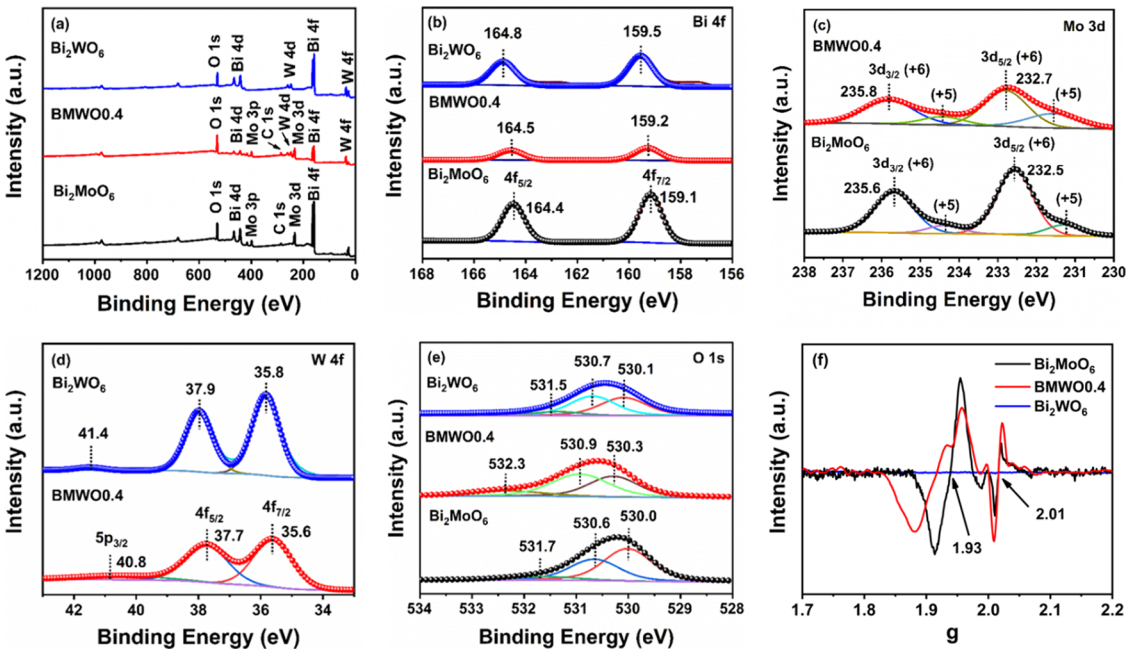

Figure 3. (a–e) XPS spectra and (f) EPR spectra of Bi_2MoO_6, BMWO0.4, and Bi_2WO_6.

and O as the constituent elements (Figure 2k–o). Moreover, atomic force microscopy (AFM) was also employed to study the effect of W-doping on Bi_2MoO_6 nanosheets (Figure S7). The thickness of Bi_2MoO_6, BMWO0.4, and Bi_2WO_6 was measured to be 156, 138, and 103 nm, respectively. The decrease in the thickness of these sheets with an increase in the concentration of W suggests a decrease in particle size, which is in accordance with the PXRD studies.

The high-resolution X-ray photoelectron spectroscopy (XPS) plots are shown in Figure 3 for Bi_2MoO_6, BMWO0.4, and Bi_2WO_6. The survey spectra of Bi_2MoO_6, BMWO0.4, and Bi_2WO_6 confirm the presence of all of the constituent elements in the samples (Figure 3a). The two peaks of Bi 4f at 164.4 and 159.1 eV represent the Bi^{3+} $4f_{5/2}$ and $4f_{7/2}$ in Bi_2MoO_6. With an increase in the concentration of W in the sample, the binding energy of these peaks increased for both BMWO0.4 and Bi_2WO_6, which were found at 164.5, 159.2, and 164.8, 159.5 eV, respectively (Figure 3b).[31] As compared to Bi_2MoO_6, the binding energy of Mo 3d peaks shift to a higher value in BMWO0.4 (Figure 3c). These peaks observed at 235.6 and 232.5 eV for Bi_2MoO_6 and 235.8 and 232.7 eV for BMWO0.4 correspond to Mo^{6+} $3d_{3/2}$ and $3d_{5/2}$, respectively.[43] The increase in the binding energy can be attributed to the incorporation of W atoms with higher electronegativity. Also, the intensity of Mo 3d peaks decreased for BMWO0.4, suggesting a decrease in its concentration. Moreover, additional peaks of Mo in +5 oxidation state were also observed in Bi_2MoO_6 and BMWO0.4 XPS spectra.[44] These peaks observed at 231.2 234.3 and 231.5 234.4 eV correspond to Mo $3d_{5/2}$ and Mo $3d_{3/2}$, respectively. Similarly, for W, the peaks corresponding to $4f_{5/2}$ and $4f_{7/2}$ have been observed at 37.7 and 35.6 eV for BMWO0.4 and at 37.9 and 35.8 eV for Bi_2WO_6 (Figure 3d).[45]

Furthermore, the O 1s spectra for Bi_2MoO_6, BMWO0.4, and Bi_2WO_6 have been studied (Figure 3e). The two peaks at 530.0 and 530.6 eV for Bi_2MoO_6 and 530.1, 530.7 eV for Bi_2WO_6 correspond to Bi–O and Mo–O/W–O bonds, respectively.[45] The incorporation of W in the crystal system leads to a decrease in electron density around O atom because of its higher electronegativity than Mo. However, the maximum shifting of peaks has been observed for BMWO0.4. The high-resolution O 1s spectra of BMWO0.4 showed peaks at 530.3 and 530.9 eV. The higher binding energy of O 1s can be attributed to the incorporation of W in the crystal system but also to the formation of oxygen vacancies. As oxygen vacancies are electron-attracting in nature which further leads to an increase in the binding energies of surrounding atoms.[46] Moreover, the peaks at 531.7 532.3, and 531.5 eV for Bi_2MoO_6, BMWO0.4, and Bi_2WO_6, respectively, correspond to the adsorbed hydrocarbons present on the surface.

To further confirm the existence of oxygen vacancies in the sample, electron paramagnetic resonance (EPR) studies were employed. It was found that in Bi_2MoO_6, some amount of oxygen vacancies was present (Figure 3f). The peak at $g = 2.01$ corresponds to the oxygen vacancies.[47] The other peak at $g = 1.93$ corresponds to the presence of Mo(V) species in the sample.[48] For BMWO0.4, the intensity of the peak at $g = 2.01$ has increased significantly more than Bi_2MoO_6 and corresponds to the increase in oxygen vacancies in it. This result is also in accordance with the increased binding energy of O 1s in BMWO0.4, indicating the presence of oxygen vacancy defects in the sample. Thus, W doping in Bi_2MoO_6 nanosheets led to an increase in defects in the sample in the form of oxygen vacancies. Additionally, the peak at $g = 1.93$ has decreased intensity for BMWO0.4 compared to Bi_2MoO_6. This decrease in the peak intensity is due to an increased concentration of W in the sample, which decreases the Mo(V) species in the sample. Besides, no EPR peak was found for Bi_2WO_6, indicating the absence of oxygen vacancies in it (Figure 3f).

3.3. Photocurrent and Photoluminescence Studies.

The photocurrent density of samples (Bi_2MoO_6, BMWO0.4, and Bi_2WO_6) was measured in dark and light conditions to study their photoelectrochemical properties (Figure S8a). The electrolyte used in this study was 0.1 M Na_2SO_4 and the potential applied was 0 V in all the cases. It was found that the

https://doi.org/10.1021/acsami.3c12563
ACS Appl. Mater. Interfaces XXXX, XXX, XXX–XXX

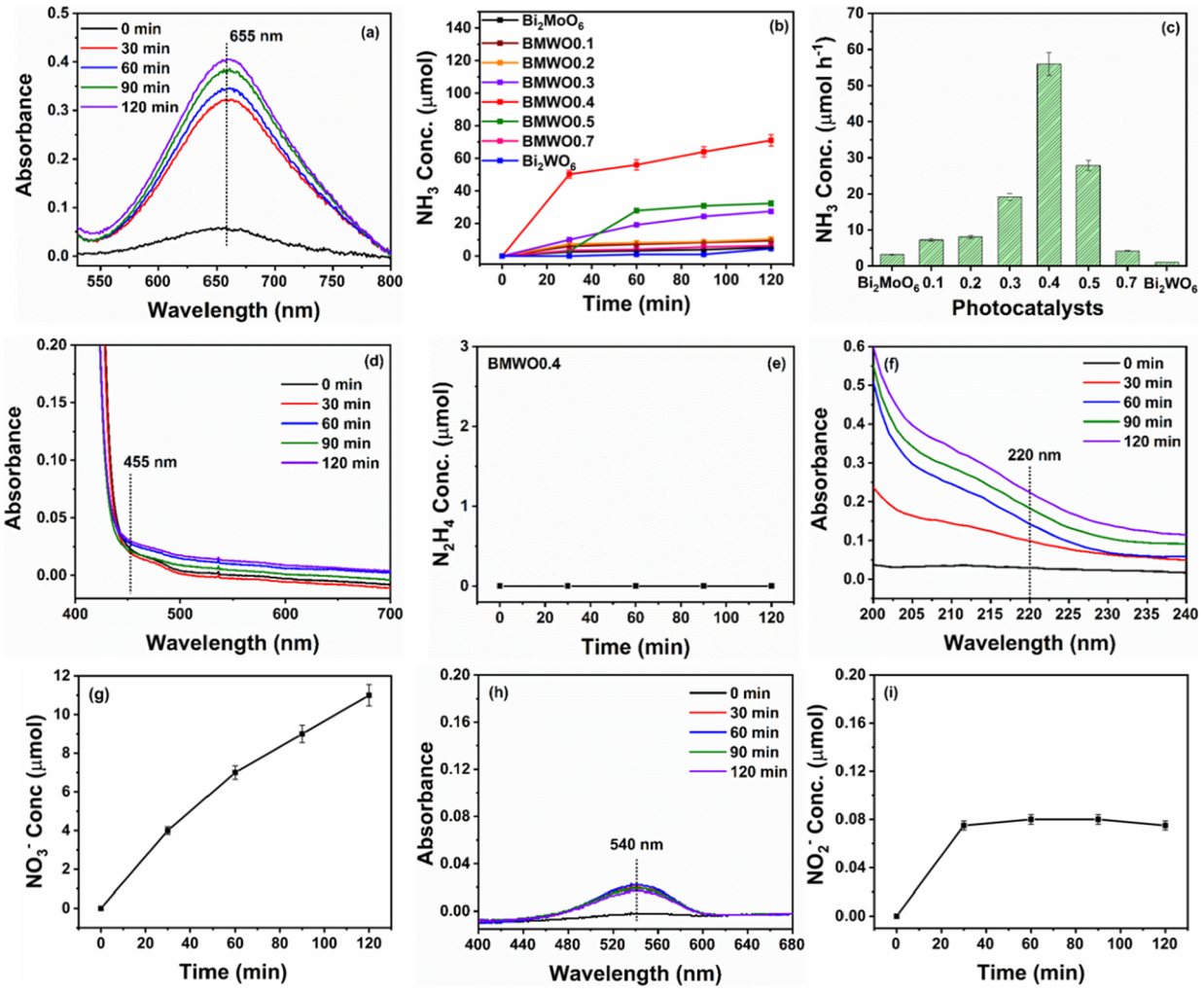

Figure 4. (a) Absorption spectra for the indophenol method using BMWO0.4; (b) photocatalytic NH_3 produced under visible light irradiation for various samples using the improved indophenol method; (c) histogram comparing the NH_3 production for various samples; (d, e) absorption spectra for the Watt−Chrisp method and N_2H_4 concentration; (f, g) absorption spectra for NO_3^- ion and plot of NO_3^- ion concentration produced at different reaction times; (h, i) absorption spectra for NO_2^- ions and plot of NO_2^- ion concentration produced at different reaction times using BMWO0.4.

current density for Bi_2MoO_6 and Bi_2WO_6 was almost the same in the presence of light but greater for BMWO0.4. The change in the current density from dark to light is maximum for BMWO0.4 as compared to Bi_2MoO_6 and Bi_2WO_6. This change in the current density is attributed to the enhanced separation of charge carriers (e^- and h^+) after the incorporation of W in Bi_2MoO_6. The effective charge separation also suggests the formation of oxygen vacancy defects in accordance with EPR spectra of BMWO0.4. These results were further supported by electrochemical impedance spectroscopic (EIS) studies (Figure S8b). The formation of a large semicircle at higher frequency indicates a large charge transfer resistance in the Nyquist plots. It can be seen in Figure S8b that there is a large curvature of the semicircle for Bi_2MoO_6 as compared to BMWO0.4 and Bi_2WO_6. This suggests that there is a maximum resistance of charge transfer and the least electron transfer potential in the sample. Furthermore, in BWMO0.4, the curvature of the semicircle is the least among all samples and suggests that there is maximum electron transfer which can further enhance the photocatalytic activity.[49,50] To check the recombination rate of charge carriers in the samples, photoluminescence (PL) spectra were recorded (Figure S8c). The intensity was found to be in the order: Bi_2MoO_6 > Bi_2WO_6 > BMWO0.4. The highest intensity of the PL spectra for Bi_2MoO_6 suggests the fastest recombination rate of charge carriers followed by Bi_2WO_6 and BMWO0.4. The lowest intensity of PL spectrum for BMWO0.4 suggests a decreased recombination rate of charge carriers in this material. Furthermore, the photoelectrochemical studies are in accordance with this result and support the same (Figure S8).

3.4. Surface Area, Thermogravimetric, and Temperature-Programmed Desorption Studies. The specific surface area was estimated using Brunauer−Emmett−Teller (BET) analysis, and the corresponding N_2 adsorption−desorption isotherm and pore size distribution plots are shown in Figure S9. The isotherm curves for all the samples were found to be of type IV. The specific surface area of Bi_2MoO_6, BMWO0.4, and Bi_2WO_6 was found to be 12.5, 25.8, and 12.6 $m^2\ g^{-1}$, respectively. The enhancement in the surface area of BMWO0.4 can be attributed to the smaller crystallite size and the porous nature. Therefore, a more irregular structure and less crystallinity of BMWO0.4 nanosheets lead to an increased surface area. Also, the presence of defects in BMWO0.4 increases the surface area, which can influence the

https://doi.org/10.1021/acsami.3c12563
ACS Appl. Mater. Interfaces XXXX, XXX, XXX−XXX

photocatalytic activity of the sample. The average pore size distribution in Bi_2MoO_6, BMWO0.4, and Bi_2WO_6 was found to be around 2−60, 2−70, and 2−40 nm, respectively. A greater number of pores with a pore size of about 67 nm were found to be in BMWO0.4. The size of all the pores suggests the mesoporous nature of the samples.[51]

The thermogravimetric studies (TGA) of Bi_2MoO_6, BMWO0.4, and Bi_2WO_6 were conducted to study the thermal stability of the samples (Figure S10a). The TGA analysis shows an approximate 2.2% total weight loss up to 900 °C in Bi_2MoO_6, which could be because of the loss of adsorbed water molecules on the surface of the sample. A similar pattern has also been seen in BMWO0.4 with a weight loss of 2.6%. For Bi_2WO_6, a total weight loss of 18.3% was observed. First, the 2.9% weight loss can be ascribed to adsorbed water molecules on the surface up to 366 °C and then further loss of 15.4% up to 900 °C can be due to the desorption of vapors like NO_2, O_2, etc., which get adsorbed on catalyst surface due to the surrounding environment.[52] All the samples were stable under thermal conditions up to 900 °C. Furthermore, the chemisorption of N_2 over the surface of the catalyst BMWO0.4 was studied using temperature-programmed desorption (TPD) (Figure S10b). The adsorption of N_2 was done over the surface of catalyst using a N_2 probe at 50 °C. Then the desorption of N_2 was checked on the surface of BMWO0.4 up to 800 °C. The peak centered at 116 °C corresponds to the physical adsorption of N_2 which generally completes up to 300 °C.[53] The desorption peaks at 304.8, 523.8, and 683.8 °C suggest strong chemisorption of N_2 over the photocatalyst surface which could be ascribed to the presence of oxygen vacancies arising from W-doping in Bi_2MoO_6 nanosheets. These peaks for chemisorbed N_2 can be attributed to three different oxygen vacancy sites in BMWO0.4 (Figure 5a). The total amount of chemisorbed N_2 over the surface of the photocatalyst was found to be 0.699 mmol g^{-1}.

3.5. Photocatalytic Nitrogen Fixation Studies. The photocatalytic performance of all of the samples was measured in pure deionized water purged with high-purity N_2 gas under visible light irradiation. There were no sacrificial agents used in this study. The determination of ammonia generated in the process was performed with UV−vis spectroscopy using an improved indophenol method.[27] Also, the formation of N_2H_4 as a side product was determined by employing the Watt-Chrisp method.[54] The concentration of photocatalytically formed NH_3 was determined by using the calibration curve of NH_3 concentration vs absorption (Figure S11a,b). A similar spectrophotometric method was adopted for the determination of N_2H_4 (Figure S11c, d). The absorption spectra pertaining to the indophenol method and Watt−Chrisp method for BMWO0.4 are shown in Figure 4a,d.

In Figure 4b, the photocatalytic ammonia production for as-synthesized samples was compared over 120 min. The total production of NH_3 for BMWO0.4 was 71 μmol in 120 min whereas the pristine Bi_2MoO_6 and Bi_2WO_6 could only produce 5.3 and 4.6 μmol, respectively. Figure S12a demonstrates the production of NH_3 under various control conditions. No production of NH_3 was observed in the absence of light (with photocatalyst) and in the absence of photocatalyst under visible light irradiation. These results confirm that the presence of the photocatalyst and light source is necessary for photocatalytic NH_3 production. When the argon gas was supplied into the reaction system instead of N_2, NH_3 production was not observed as seen in Figure S12a. Also, no involvement of atmospheric NH_3 was seen in the control reactions. The comparison of NH_3 production per hour in all the samples has been done in Figure 4c. It was found that the photocatalytically produced NH_3 was at its maximum for BMWO0.4 which was 56 μmol h^{-1} in comparison to Bi_2MoO_6 (3 μmol h^{-1}) and Bi_2WO_6 (1 μmol h^{-1}) (Figure 4c). Also, the NH_3 produced by all the samples has been converted to μmol g^{-1} h^{-1} and shown in the Figure S12b. To check the accuracy of the indophenol method, Nessler's reagent method was also employed to detect the ammonia production after 120 min (Figure S13). The amount of ammonia detected was found to be 67 μmol after 120 min. While for the indophenol method, the amount of ammonia produced was estimated to be 71 μmol in the same duration of time. This indicates that the ammonia production detected using both of these methods (indophenol and Nessler's reagent) are almost similar, underscoring the reliability and accuracy of the employed techniques. In addition, the Watt−Chrisp method was employed to observe any production of N_2H_4 in the reaction mixture. There was no production of N_2H_4 observed throughout the reaction (Figure 4e). Also, the absence of N_2H_4 in the reaction mixture gives insight into the mechanism of ammonia formation, wherein the hydrogenation of the distal nitrogen atom takes place instead of both nitrogen atoms.[13,55] Moreover, the turnover frequency (TOF) calculated for this process by using BMWO0.4 was found to be 0.162 h^{-1}. In addition, the comparison of the photocatalytic performance of BMWO0.4 with other similar doped materials is provided in Table S3, which reveals its higher or comparable N_2 fixation ability to other previously reported materials. All these literature reports specifically mention the reduction of N_2 into NH_3 in pure water, but there is no mention of oxidized products like NO_3^- and NO_2^-. In this work, simultaneous identification and quantification of the NO_3^- and NO_2^- ions have been done. As many literature reports are not available on simultaneous production of NH_3, NO_3^- and NO_2^- ions, this work makes it more significant in the field of photocatalytic nitrogen fixation.

To further confirm the formation of NH_3 in the reaction mixture, mass spectrometry was employed. The mass spectrum of pure water was also recorded, in which no such peak was observed signifying the absence of NH_3 as an impurity (Figure S14a). Also, it infers that there is no interference of atmospheric ammonia with the reaction mixture. To identify the peaks of products formed in the indophenol test, the samples of standard NH_3 solution were tested through the indophenol method and subjected to mass spectroscopy (Figure S14b−d). Different intensities of the m/z = 297.06 peak are related to different concentrations of NH_3 in the solution and to the formation of indophenol dye. The structure of the molecule with an exact mass of 298.05 is provided in the Supporting Information (Figure S15). To ensure that the formation of NH_3 takes place after purging of N_2 gas only, $^{15}N_2$ gas was supplied to the reaction mixture. The peak at m/z = 298.06 nm corresponds to the indophenol product obtained from $^{15}N_2$ gas. The intensity ratio of the peaks at m/z = 297.06 and 298.06 was 6.86 for $^{14}N_2$ gas and 5.94 for $^{15}N_2$ gas (Figure S16). The decrease in the intensity ratio of $^{15}N_2$ indicates the increase in the intensity of the peak at m/z = 298.06. This corresponds to the increase in the formation of indophenol using $^{15}N_2$ gas (Figure S17a,b). Furthermore, the reaction mixture of purged $^{14}N_2$ gas was taken and subjected to ^1H NMR studies. The triplet corresponding to I = 1 of ^{14}N

https://doi.org/10.1021/acsami.3c12563
ACS Appl. Mater. Interfaces XXXX, XXX, XXX−XXX

Scheme 2. (a) Schematic Illustration of the Proposed Photocatalytic Mechanism over the Surface of BMWO0.4; (b) Schematic Illustration Depicting the Proposed Pathway for NH_3 Formation over the BMWO0.4 Surface

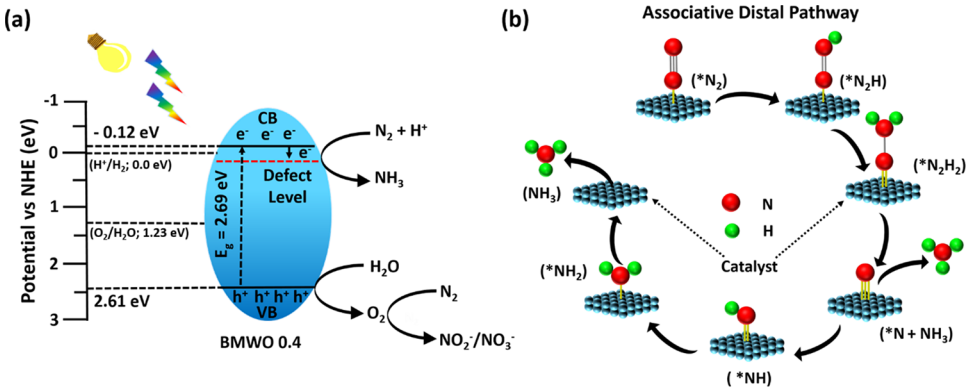

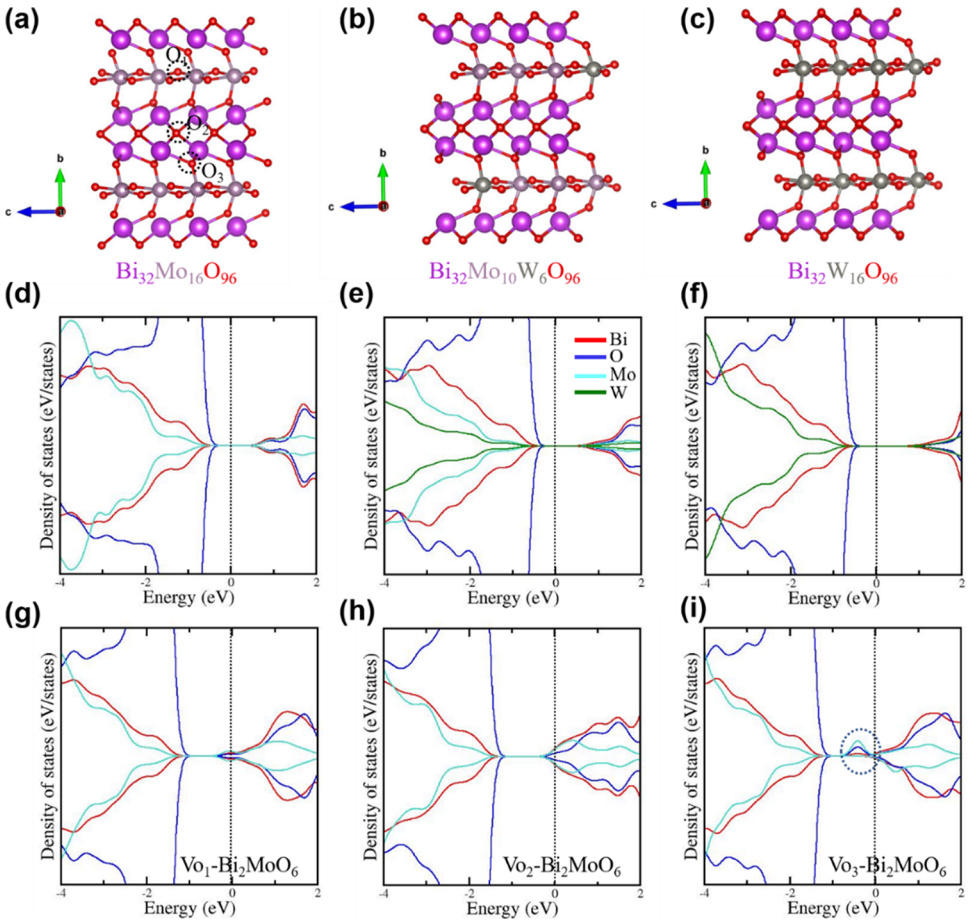

Figure 5. Optimized structure of (a) pristine system $Bi_{32}Mo_{16}O_{96}$, (b) Mo substituted $Bi_{32}Mo_{10}W_6O_{96}$ and (c) $Bi_{32}W_{16}O_{96}$. Partial density of states (pDOS) of (d) pristine $Bi_{32}Mo_{16}O_{96}$, (e) $Bi_{32}Mo_{10}W_6O_{96}$, (f) $Bi_{32}W_{16}O_{96}$, (g) defected Bi_2MoO_6 with an O-vacancy at the O_1-site (V_{O1}-Bi_2MoO_6), (h) defected Bi_2MoO_6 with an O-vacancy at the O_2-site (V_{O2}-Bi_2MoO_6), and (i) defected Bi_2MoO_6 with an O-vacancy at the O_3-site (V_{O3}-Bi_2MoO_6).

between 6.56 and 6.86 ppm was found, which further confirms the formation of NH_3 (Figure S17c). The *J*-value of the peaks came out to be 52.2 Hz.

In addition, the concentration of photocatalytically formed oxidized products (utilizing the holes), including NO_3^- and NO_2^- ions was also determined by using the calibration curves of respective ion concentration vs absorption (Figure S18a–d). The UV–vis absorption spectra of NO_3^- and NO_2^- ions and their concentrations detected in the reaction mixture for BMWO0.4 are shown in Figure 4f–i. The amount of NO_3^- ions produced for BMWO0.4 was determined to be 11 μmol after 120 min, while that of NO_2^- was only 0.075 μmol for the same period. Although the amount of NO_2^- ions produced is very less, the UV–vis spectra for NO_2^- ions showed a decreased absorption intensity which suggests the further oxidation of NO_2^- ions into NO_3^- ions. These results also suggest the nonlinear production of NH_3 from 60 min (56 μmol) to 120 min (71 μmol) because of the simultaneous

https://doi.org/10.1021/acsami.3c12563
ACS Appl. Mater. Interfaces XXXX, XXX, XXX–XXX

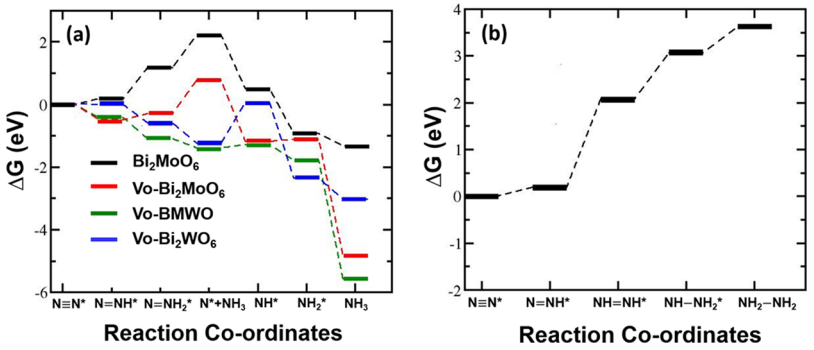

Figure 6. (a) Variation of the Gibbs free energy of formation (ΔG) for N_2 fixation over the (010) surface for pristine (BMO) and defected configurations with various reaction steps involved in the N_2 fixation for the distal pathway. Here, V_O denotes a single O-vacancy at the surface. BMO, BMWO, and BWO represent $Bi_{32}Mo_{16}O_{96}$, $Bi_{32}Mo_{10}W_6O_{96}$, and $Bi_{32}W_{16}O_{96}$, respectively. (b) Variation of the Gibbs free energy of formation (ΔG) for N_2 fixation over the (010) surface for pristine (BMO) for an alternative pathway.

production of oxidized products (NO_3^-, NO_2^-) in the reaction mixture.

The photocatalytic mechanism of nitrogen fixation is given below (Scheme 2a). In addition, the absence of N_2H_4 in the reaction mixture suggests the formation of NH_3 took place by a dissociative distal pathway which is given in Scheme 2b. In brief, after the incorporation of W in the Bi_2MoO_6 nanosheets, it has been found that both VB and CB shift toward the lower potential, which is in accordance with previous literature.[31] The CB position (−0.12 eV) of BMWO0.4 is above the water reduction potential (H^+/H_2; 0.0 eV) and VB position (2.57 eV) is located below the water oxidation potential (O_2/H_2O; 1.23 eV).[56] A more negative position of CB as compared to the reduction potential of water and a more positive position of VB as compared to the oxidation potential of water in BMWO0.4 make it suitable for photocatalytic nitrogen fixation. Hence, it leads to the simultaneous production of the reduced product (NH_3) attributable to the photogenerated electrons and oxidized products (NO_3^- and NO_2^-) attributable to the photogenerated holes. Furthermore, some oxygen vacancy sites are also formed after the introduction of W in Bi_2MoO_6 nanosheets, as evidenced by EPR studies. These oxygen vacancies in the sample act as electron trapping sites and hence, reduce the recombination rate of charge carriers. Also, surface oxygen vacancies help in activating the N_2 molecules by reducing them and chemically adsorbing them on the photocatalyst surface.[57] The maximum generation of oxygen vacancies and the narrow band gap in BMWO0.4 could be the reasons for its highest photocatalytic activity. Moreover, the narrow band gap helps to achieve the effective absorption of visible light.

Photostability and recyclability are the two main aspects of a photocatalyst. The recyclability of BMWO0.4 was checked up to six cycles (Figure S19a). After each cycle, the catalyst was recovered, washed, and dried, and then it was subjected to the next cycle of recyclability. It was found that the production of NH_3 decreased from 71 to 57 μmol after six cycles in 120 min. The PXRD of the photocatalyst before and after use is shown in Figure S19b which shows the excellent stability of the photocatalyst even after multiple cycles. The EPR spectra of BMWO0.4 was also taken before and after the recyclability study and a small decrease in the peak intensity of the recycled sample was observed (Figure S19c). The decreased intensity of the EPR signal can be attributed to the blocking of oxygen vacancy sites due to the adsorption of atmospheric oxygen or other hydrocarbons. The blocking of oxygen vacancy sites after multiple cycles can lead to a decreased number of surface-active sites, which affects the photocatalytic activity of the BMWO0.4 catalyst.

Furthermore, density functional theory (DFT) calculations were performed to get insights into the electronic structures of Bi_2MoO_6, BMWO0.4, and Bi_2WO_6. The partial density of states (pDOS) was calculated for the pristine and W-doped configurations with and without an O-vacancy (V_O) to reveal the effect of the defects on the electronic structure. Figure 5a–c shows the optimized structures of the pristine ($Bi_{32}Mo_{16}O_{96}$), W-doped configuration ($Bi_{32}Mo_{10}W_6O_{96}$), and $Bi_{32}W_{16}O_{96}$. In $Bi_{32}Mo_{16}O_{96}$, O-2p contributes maximum to the VBM and CBm is contributed by the Bi6p, Mo-4d, and O-2p orbitals (Figure 5d). In the absence of any unpaired electron, the states are symmetric with respect to spin alignments (i.e., spin-up and spin-down). Here, the Fermi level is set to zero (shown with a dotted black line). Similarly, in the case of $Bi_{32}Mo_{10}W_6O_{96}$ and $Bi_{32}W_{16}O_{96}$ the states are symmetric, and the system is p-type in nature (Figure 5e,f). In Figure 5g–i, we have shown the pDOS of the pristine system with one O-vacancy at the O_1-site (Vo_1), an O-vacancy at the O_2-site (V_{O2}) and an O-vacancy at the O_3-site (Vo_3), respectively. It is observed that for V_O at the O_1 and O_2 sites, the states remain symmetric, but the band gap decreases due to the introduction of delocalized states near CBm due to the presence of O-vacancy defects (Figure 5g,h). However, on doing V_O at the O_3 site, we can clearly see localized energy levels occurring near the CBm due to strong hybridization of the Mo-4d and the O-2p orbitals (Figure 5i). Moreover, on doing V_O (at the $O_1/O_2/O_3$-site), the Fermi level rises to CBm, accompanied by a realization that the system becomes n-type on doing V_O. Similar results were observed on doing V_O at different sites in Mo substituted configuration, i.e., $Bi_{32}Mo_{10}W_6O_{96}$ (Figure S20). In the case of a system with V_O, an additional photo absorption may take place due to the transition of the electron localized in the defect state to the CBm. Moreover, the systems with the O vacancy exhibit reduced band gaps in comparison to the pristine, which is favorable for the creation of photoinduced charge carriers. Since the Perdew–Burke–Ernzerhof (PBE) functional underestimates the band gap, we calculated the band gap using HSE06 hybrid functional for $Bi_{32}Mo_{16}O_{96}$, $Bi_{32}Mo_{10}W_6O_{96}$, and $Bi_{32}W_{16}O_{96}$ i.e, 2.35, 2.27, and 3.20 eV, respectively. Though the theoretical band gaps calculated using HSE06 do not exactly match with the experimental values, a decrease in the band gap on doing partial substitution at Mo sites with W is consistent with experimentally observed results.

https://doi.org/10.1021/acsami.3c12563
ACS Appl. Mater. Interfaces XXXX, XXX, XXX–XXX

To explore the N_2 fixation with different systems (pristine or defected configurations) using the DFT approach, here we determined the Gibbs free energy of the formation (ΔG). In photocatalytic N_2 fixation, the successive hydrogenation of the adsorbed N_2 on the surface of the catalyst. First, we modeled surfaces, i.e., (010) surfaces with BiO-termination for pristine and W-doped configurations (either partially or completely with W) to determine the ΔG values (for details, see the computational details section in the Supporting Information). In the case of a pristine system, most of the steps involved in N_2 fixation are endothermic and the step (in which the first molecule of NH_3 is produced) is the most endothermic reaction step (Figure 6a). This shows that in the case of the pristine system, the least amount of NH_3 production will take place. On the other hand, on doing an O-vacancy (V_O) at the surface of the pristine (V_O-BMO), the initial steps involved in N_2 fixation are exothermic, and the step which involves the production of NH_3 is endothermic but less in comparison to the pristine. In the case of W-doped substituted configuration with O-vacancy at the surface (V_O-BMWO), all the N_2 fixation steps are exothermic and the step which involves the NH_3 production is the most exothermic, which conveys that a large amount NH_3 will be evolved in case of V_O-BMWO. From the ΔG variation (Figure 6a), in the case of V_O-BWO (system with O-vacancy at the surface and Mo completely substituted with W), it can be inferred that less NH_3 will be evolved during N_2 fixation on the surface of Mo completely substituted configurations than in case of partially substituted configurations. We also checked the variation of ΔG for the N_2 fixation along the alternative path for the pristine system and it was observed that N_2 fixation along the alternative path is more endothermic (Figure 6b). Hence, the alternative path is not the preferred path for N_2 fixation. Overall, the obtained values of ΔG suggest that a partially Mo-substituted configuration with an O-vacancy is most favorable for N_2 fixation. Hence, it can be inferred that the oxygen vacancy sites in the partially substituted Mo configuration act as active sites for photocatalytic nitrogen fixation. Additionally, we observed that the N−N bond length was increased to 1.23 Å from 1.09 Å on adsorption of the N_2 molecule at the O-vacancy in comparison to the pristine system. This was due to more charge transfer from the system to N_2 molecule when it is adsorbed at O-vacancy.[58] The optimized structures for N_2 absorbed on Bi_2MoO_6 and V_O-Bi_2MoO_6 are shown in Figure S21. The elongation can be attributed to a substantial charge transfer from the system to the N_2 molecule when it is adsorbed at the O-vacancy site. To depict this charge transfer, we have provided charge difference density results (Figure S21). In the case of N_2 adsorbed on V_O-Bi_2MoO_6, we noticed a higher localization of charge near the N_2 molecule compared to that when N_2 is adsorbed on Bi_2MoO_6. This localized charge distribution confirms the enhanced charge transfer from the system to the N_2 molecule when it is adsorbed at the O-vacancy. This weakens the N−N bond and, hence, enhances the activation of the N_2 molecule for further photocatalytic reaction for N_2 fixation.

Based on theoretical and experimental results, we can say that W-doping in Bi_2MoO_6 not only introduced lattice distortion but also generated oxygen vacancies on the surface of the photocatalyst. The superior activity of BMWO0.4 can be ascribed to an increased number of surface defects, which helped in the adsorption of N_2 molecules as well as decreased the recombination of charge carriers. This chemisorption of N_2 over the surface of the photocatalyst enables the formation of NH_3 and NO_3^-. Moreover, the reaction pathway, which is a dissociative distal pathway involved in the NH_3 formation, was confirmed by both theoretical and experimental studies.

4. CONCLUSIONS

In summary, we synthesized W-doped Bi_2MoO_6 nanosheets where W has been doped in various molar ratios, and their effect on morphology and photocatalytic activity has been studied. The effect on morphology was confirmed by SEM, TEM, and AFM analysis where the thickness of nanosheets was decreased with W-doping. Furthermore, doping of W leads to the generation of oxygen vacancies in the samples as confirmed by EPR and XPS studies. In addition, the effect of doping on bandgap and valence band values has been studied by DRS, UPS, and REELS techniques. These sheets were employed for photocatalytic nitrogen fixation under visible light irradiation. It was found that one of the catalysts having the optimal amount of W-doping (BMWO0.4) was the best photocatalyst with the highest NH_3 production of (56 μmol h^{-1}) in 120 min as compared to pristine Bi_2MoO_6 (3 μmol h^{-1}) and Bi_2WO_6 (1 μmol h^{-1}). The best BMWO0.4 photocatalyst also showed the simultaneous production of NO_3^- ions at a rate of 7 μmol h^{-1}. This increase in photocatalytic activity can be attributed to oxygen vacancy defects produced due to lattice distortions in W-doped Bi_2MoO_6. This provides more active sites as well as decreases the recombination of photogenerated charge carriers, thereby enhancing the photocatalytic activity. Moreover, theoretical investigations agree well with the experimental results. Thus, the present work provides crucial insights into the defect-engineered photocatalysts and their application in light-driven nitrogen fixation. This work further elucidates the fabrication of efficient photocatalysts by doping, which can tune both the nanostructure and band gap, paving the way for the developments of advanced defect-rich, light-harvesting materials.

■ ASSOCIATED CONTENT

Supporting Information

The Supporting Information is available free of charge at https://pubs.acs.org/doi/10.1021/acsami.3c12563.

Materials characterization, calculated crystallite size, lattice strain, and lattice parameters, FTIR spectra, images of samples, UV−vis absorption spectra and Kubelka−Munk plots, TEM and HRTEM images of Bi_2MoO_6 and Bi_2WO_6, AFM images of of Bi_2MoO_6, BMWO0.4, and Bi_2WO_6, photocurrent and Nyquist plots of Bi_2MoO_6, BMWO0.4, and Bi_2WO_6, photoluminescence spectra of Bi_2MoO_6, BMWO0.4, and Bi_2WO_6, BET plots of Bi_2MoO_6, BMWO0.4, and Bi_2WO_6, TGA and TPD curves, absorption spectra of standard solutions, calibration curves indophenol and Watt−Chrisp methods, mass spectra of pure water and standard NH_3 solutions, molecular structure of the obtained compound in mass spectroscopy, mass spectra of samples after purging $^{14}N_2$ and $^{15}N_2$ gas, mass fragments found using $^{14}N_2$, $^{15}N_2$, NMR spectra, absorption spectra of standard solutions and calibration curves for NO_3^- and NO_2^- ions, absorption spectra of standard solutions and calibration curve for NH_3 using Nessler's reagent, plots for recyclability of BMWO0.4,

https://doi.org/10.1021/acsami.3c12563
ACS Appl. Mater. Interfaces XXXX, XXX, XXX−XXX

PXRD and EPR of catalyst before and after use, calculation of turnover frequency for BMWO0.4, and optimized structure and charge density difference contours (PDF)

AUTHOR INFORMATION

Corresponding Authors

Abhijit Patra − *Department of Chemistry, Indian Institute of Science Education and Research Bhopal, Bhopal, Madhya Pradesh 462066, India;* orcid.org/0000-0003-3144-1813; Email: abhijit@iiserb.ac.in

Saswata Bhattacharya − *Department of Physics, Indian Institute of Technology Delhi, New Delhi 110016, India;* orcid.org/0000-0002-4145-4899; Email: saswata@physics.iitd.ac.in

Venkata Krishnan − *School of Chemical Sciences and Advanced Materials Research Center, Indian Institute of Technology Mandi, Mandi, Himachal Pradesh 175075, India;* orcid.org/0000-0002-4453-0914; Email: vkn@iitmandi.ac.in

Authors

Manisha Sharma − *School of Chemical Sciences and Advanced Materials Research Center, Indian Institute of Technology Mandi, Mandi, Himachal Pradesh 175075, India*

Ashish Kumar − *Department of Chemistry, Sardar Patel University Mandi, Mandi, Himachal Pradesh 175001, India;* orcid.org/0000-0003-3527-4952

Deepika Gill − *Department of Physics, Indian Institute of Technology Delhi, New Delhi 110016, India*

Shilpi Jaiswal − *Department of Chemistry, Indian Institute of Science Education and Research Bhopal, Bhopal, Madhya Pradesh 462066, India*

Complete contact information is available at: https://pubs.acs.org/10.1021/acsami.3c12563

Author Contributions

Conceptualization: M.S. and V.K.; methodology (materials preparation, characterization, and catalytic studies): M.S., A.K., and V.K.; methodology (computational studies): D.G. and S.B.; methodology (EPR studies): S.J. and A.P.; data analysis for respective studies: M.S., A.K., D.G., and S.J.; writing—first draft: M.S., A.K., D.G., and S.J.; writing—review and editing: all authors; supervision and funding acquisition: A.P., S.B., and V.K.; A.K., D.G., and S.J. contributed equally to this work.

Notes

The authors declare no competing financial interest.

ACKNOWLEDGMENTS

We are thankful to Advanced Material Research Centre (AMRC), IIT Mandi for laboratory and characterization facilities. V.K. gratefully acknowledges DST-SERB (grant no. CRG/2022/003559) for financial support. M.S. thanks the Ministry of Education (MoE), India for her doctoral research fellowship. A.K. thanks DST-SERB (project no. SUR/2022/003038) for financial support. S.J. acknowledges the Council of Scientific Industrial Research (CSIR), India for senior research fellowship. A.P. thanks DST-SERB (grant no. CRG/2021/008526) for the financial support. D.G. acknowledges University Grants Commission (UGC), India for senior research fellowship. S.B. acknowledges the financial support from DST-SERB (grant no. CRG/2019/000647). We acknowledge the High-Performance Computing (HPC) facility at IIT Delhi for computational resources.

REFERENCES

(1) Kumar, A.; Kumar, A.; Krishnan, V. Perovskite oxide based materials for energy and environment-oriented photocatalysis. *ACS Catal.* **2020**, *10* (17), 10253−10315.

(2) Xia, P.; Pan, X.; Jiang, S.; Yu, J.; He, B.; Ismail, P. M.; Bai, W.; Yang, J.; Yang, L.; Zhang, H.; Cheng, M.; Li, H.; Zhang, Q.; Xiao, C.; Xie, Y. Designing a Redox Heterojunction for Photocatalytic "Overall Nitrogen Fixation" under Mild Conditions. *Adv. Mater.* **2022**, *34* (28), No. 2200563.

(3) Liu, Q.-Y.; Wang, H.-D.; Tang, R.; Cheng, Q.; Yuan, Y.-J. Rutile TiO_2 Nanoparticles with Oxygen Vacancy for Photocatalytic Nitrogen Fixation. *ACS Applied Nano Materials* **2021**, *4* (9), 8674−8679.

(4) Xu, F.; Wu, F.; Zhu, K.; Fang, Z.; Jia, D.; Wang, Y.; Jia, G.; Low, J.; Ye, W.; Sun, Z.; Gao, P.; Xiong, Y. Boron Doping and High Curvature in Bi Nanorolls for Promoting Photoelectrochemical Nitrogen Fixation. *Appl. Catal., B* **2021**, *284*, No. 119689.

(5) Lan, R.; Irvine, J. T.; Tao, S. Ammonia and Related Chemicals as Potential Indirect Hydrogen Storage Materials. *Int. J. Hydrogen Energy* **2012**, *37* (2), 1482−1494.

(6) Kumar, A.; Krishnan, V. Vacancy Engineering in Semiconductor Photocatalysts: Implications in Hydrogen Evolution and Nitrogen Fixation Applications. *Adv. Funct. Mater.* **2021**, *31* (28), No. 2009807.

(7) Shi, R.; Zhao, Y.; Waterhouse, G. I.; Zhang, S.; Zhang, T. Defect Engineering in Photocatalytic Nitrogen Fixation. *ACS Catal.* **2019**, *9* (11), 9739−9750.

(8) Smith, C.; Hill, A. K.; Torrente-Murciano, L. Current and Future Role of Haber−Bosch Ammonia in a Carbon-Free Energy Landscape. *Energy Environ. Sci.* **2020**, *13* (2), 331−344.

(9) Kumar, A.; Sharma, M.; Sheoran, S.; Jaiswal, S.; Patra, A.; Bhattacharya, S.; Krishnan, V. Tailoring Defects in $SrTiO_3$ by One Step Nanoarchitectonics for Realizing Photocatalytic Nitrogen Fixation in Pure Water. *Nanoscale* **2023**, *15*, 11667.

(10) Zhang, W.; Xing, P.; Zhang, J.; Chen, L.; Yang, J.; Hu, X.; Zhao, L.; Wu, Y.; He, Y. Facile Preparation of Novel Nickel Sulfide Modified $KNbO_3$ Heterojunction Composite and its Enhanced Performance in Photocatalytic Nitrogen Fixation. *J. Colloid Interface Sci.* **2021**, *590*, 548−560.

(11) Li, G.; Yang, W.; Gao, S.; Shen, Q.; Xue, J.; Chen, K.; Li, Q. Creation of Rich Oxygen Vacancies in Bismuth Molybdate Nanosheets to Boost the Photocatalytic Nitrogen Fixation Performance under Visible Light Illumination. *Chemical Engineering Journal* **2021**, *404*, No. 127115.

(12) Huang, H.; Wang, X.-S.; Philo, D.; Ichihara, F.; Song, H.; Li, Y.; Li, D.; Qiu, T.; Wang, S.; Ye, J. Toward Visible-Light-Assisted Photocatalytic Nitrogen Fixation: A Titanium Metal Organic Framework with Functionalized Ligands. *Applied Catalysis B: Environmental* **2020**, *267*, No. 118686.

(13) Li, G.; Yang, W.; Gao, S.; Shen, Q.; Xue, J.; Chen, K.; Li, Q. Creation of Rich Oxygen Vacancies in Bismuth Molybdate Nanosheets to Boost the Photocatalytic Nitrogen Fixation Performance under Visible Light Illumination. *Chemical Engineering Journal* **2021**, *404*, No. 127115.

(14) Zhao, Y.; Zhao, Y.; Shi, R.; Wang, B.; Waterhouse, G. I.; Wu, L. Z.; Tung, C. H.; Zhang, T. Tuning Oxygen Vacancies in Ultrathin TiO_2 Nanosheets to Boost Photocatalytic Nitrogen Fixation up to 700 nm. *Adv. Mater.* **2019**, *31* (16), No. 1806482.

(15) Zhang, N.; Gao, C.; Xiong, Y. Defect Engineering: A Versatile Tool for Tuning the Activation of Key Molecules in Photocatalytic Reactions. *Journal of Energy Chemistry* **2019**, *37*, 43−57.

(16) Aono, M.; Ariga, K. The Way to Nanoarchitectonics and the Way of Nanoarchitectonics. *Adv. Mater.* **2016**, *28* (6), 989−992.

(17) Lan, M.; Wang, Y.; Dong, X.; Yang, F.; Zheng, N.; Wang, Y.; Ma, H.; Zhang, X. Controllable Fabrication of Sulfur-Vacancy-Rich Bi_2S_3 Nanorods with Efficient Near-Infrared Light Photocatalytic for Nitrogen Fixation. *Appl. Surf. Sci.* **2022**, *591*, No. 153205.

(18) Ma, T.; Yang, C.; Guo, L.; Soomro, R. A.; Wang, D.; Xu, B.; Fu, F. Refining Electronic Properties of Bi_2MoO_6 by In-Doping for Boosting Overall Nitrogen Fixation via Relay Catalysis. *Applied Catalysis B: Environmental* **2023**, *330*, No. 122643.
(19) Zheng, Y.; Zhou, T.; Zhao, X.; Pang, W. K.; Gao, H.; Li, S.; Zhou, Z.; Liu, H.; Guo, Z. Atomic Interface Engineering and Electric-Field Effect in Ultrathin Bi_2MoO_6 Nanosheets for Superior Lithium Ion Storage. *Adv. Mater.* **2017**, *29* (26), No. 1700396.
(20) Sharma, M.; Kumar, A.; Krishnan, V. Influence of Oxygen Vacancy Defects on Aurivillius Phase Layered Perovskite Oxides of Bismuth Towards Photocatalytic Environmental Remediation. *Nanotechnology* **2022**, *33* (27), 275702.
(21) Di, J.; Zhao, X.; Lian, C.; Ji, M.; Xia, J.; Xiong, J.; Zhou, W.; Cao, X.; She, Y.; Liu, H. Atomically-Thin Bi_2MoO_6 Nanosheets with Vacancy Pairs for Improved Photocatalytic CO_2 Reduction. *Nano Energy* **2019**, *61*, 54−59.
(22) Chen, Y.; Yang, W.; Gao, S.; Sun, C.; Li, Q. Synthesis of Bi_2MoO_6 Nanosheets with Rich Oxygen Vacancies by Postsynthesis Etching Treatment for Enhanced Photocatalytic Performance. *ACS Applied Nano Materials* **2018**, *1* (7), 3565−3578.
(23) Meng, Q.; Lv, C.; Sun, J.; Hong, W.; Xing, W.; Qiang, L.; Chen, G.; Jin, X. High-Efficiency Fe-Mediated Bi_2MoO_6 Nitrogen-Fixing Photocatalyst: Reduced Surface Work Function and Ameliorated Surface Reaction. *Applied Catalysis B: Environmental* **2019**, *256*, No. 117781.
(24) Xue, X.; Chen, R.; Yan, C.; Hu, Y.; Zhang, W.; Yang, S.; Ma, L.; Zhu, G.; Jin, Z. Efficient Photocatalytic Nitrogen Fixation under Ambient Conditions Enabled by the Heterojunctions of n-type Bi_2MoO_6 and Oxygen-Vacancy-Rich p-type BiOBr. *Nanoscale* **2019**, *11* (21), 10439−10445.
(25) Arif, M.; Zhang, M.; Qiu, B.; Yao, J.; Bu, Q.; Ali, A.; Muhmood, T.; Hussian, I.; Liu, X.; Zhou, B.; Wang, X. Synergistic Effect of Ultrathin Thickness and Surface Oxygen Vacancies in High-Efficiency Ti-mediated Bi_2MoO_6 for Immense Photocatalytic Nitrofurantoin Degradation and Cr (VI) Reduction. *Appl. Surf. Sci.* **2021**, *543*, No. 148816.
(26) Nazemi, M.; El-Sayed, M. A. Plasmon-Enhanced Photo (Electro) Chemical Nitrogen Fixation under Ambient Conditions using Visible Light Responsive Hybrid Hollow Au-Ag_2O Nanocages. *Nano Energy* **2019**, *63*, No. 103886.
(27) Zhao, X.; Lan, X.; Yu, D.; Fu, H.; Liu, Z.; Mu, T. Deep Eutectic-Solvothermal Synthesis of Nanostructured Fe_3S_4 for Electrochemical N_2 Fixation under Ambient Conditions. *Chem. Commun.* **2018**, *54* (92), 13010−13013.
(28) Zhang, N.; Li, L.; Shao, Q.; Zhu, T.; Huang, X.; Xiao, X. Fe-Doped BiOCl Nanosheets with Light-Switchable Oxygen Vacancies for Photocatalytic Nitrogen Fixation. *ACS Applied Energy Materials* **2019**, *2* (12), 8394−8398.
(29) Sharma, M.; Kumar, A.; Krishnan, V. Influence of Oxygen Vacancy Defects on Aurivillius Phase Layered Perovskite Oxides of Bismuth Towards Photocatalytic Environmental Remediation. *Nanotechnology* **2022**, *33* (27), 275702.
(30) Zhang, L.; Man, Y.; Zhu, Y. Effects of Mo Replacement on the Structure and Visible-Light-Induced Photocatalytic Performances of Bi_2WO_6 Photocatalyst. *ACS Catal.* **2011**, *1* (8), 841−848.
(31) Xie, Y.; Liu, D.; Wang, B.; Li, D.; Yan, Z.; Chen, Y.; Shen, J.; Zhang, Z.; Wang, X. Monolayer $Bi_2W_{1-x}Mo_xO_6$ Solid Solutions for Structural Polarity to Boost Photocatalytic Reduction of Nitrobenzene under Visible Light. *ACS Sustainable Chem. Eng.* **2021**, *9* (6), 2465−2474.
(32) Hardcastle, F. D.; Wachs, I. E. Molecular Structure of Molybdenum Oxide in Bismuth Molybdates by Raman Spectroscopy. *J. Phys. Chem.* **1991**, *95* (26), 10763−10772.
(33) Phuruangrat, A.; Jitrou, P.; Dumrongrojthanath, P.; Ekthammathat, N.; Kuntalue, B.; Thongtem, S.; Thongtem, T. Hydrothermal Synthesis and Characterization of Bi_2MoO_6 Nanoplates and their Photocatalytic Activities *J. Nanomater.* 2013, *2013*, 789705, DOI: 10.1155/2013/789705
(34) Salari, H. Facile Synthesis of New Z-scheme Bi_2WO_6/Bi_2MoO_6 p−n Junction Photocatalysts with High Photocatalytic Activity: Structure, Kinetics and Mechanism Approach. *Mater. Res. Bull.* **2020**, *131*, No. 110979.
(35) Phuruangrat, A.; Putdum, S.; Dumrongrojthanath, P.; Thongtem, S.; Thongtem, T. Hydrothermal Synthesis of Bi_2MoO_6 Visible-Light-Driven Photocatalyst *J. Nanomater.* 2015, *2015*, 789705, DOI: 10.1155/2015/135735.
(36) Raizada, P.; Kumari, J.; Shandilya, P.; Dhiman, R.; Singh, V. P.; Singh, P. Magnetically Retrievable Bi_2WO_6/Fe_3O_4 Immobilized on Graphene Sand Composite for Investigation of Photocatalytic Mineralization of Oxytetracycline and Ampicillin. *Process Safety Environ. Protect.* **2017**, *106*, 104−116.
(37) Phuruangrat, A.; Keereesaensuk, P.-O.; Karthik, K.; Dumrongrojthanath, P.; Ekthammathat, N.; Thongtem, S.; Thongtem, T. Synthesis and Characterization Ag Nanoparticles Supported on Bi_2WO_6 Nanoplates for Enhanced Visible-Light-Driven Photocatalytic Degradation of Rhodamine B. *Journal of Inorganic and Organometallic Polymers and Materials* **2020**, *30* (4), 1033−1040.
(38) Zhou, L.; Yu, M.; Yang, J.; Wang, Y.; Yu, C. Nanosheet-Based $Bi_2Mo_xW_{1-x}O_6$ Solid Solutions with Adjustable Band Gaps and Enhanced Visible-Light-Driven Photocatalytic Activities. *J. Phys. Chem. C* **2010**, *114* (44), 18812−18818.
(39) Sun, W.; Meng, S.; Zhang, S.; Zheng, X.; Ye, X.; Fu, X.; Chen, S. Insight into the Transfer Mechanisms of Photogenerated Carriers for Heterojunction Photocatalysts with the Analogous Positions of Valence Band and Conduction Band: A Case Study of ZnO/TiO_2. *J. Phys. Chem. C* **2018**, *122* (27), 15409−15420.
(40) Gao, J.; Liu, C.; Wang, F.; Jia, L.; Duan, K.; Liu, T. Facile Synthesis of Heterostructured WS_2/Bi_2MoO_6 as high-performance visible-light-driven photocatalysts. *Nanoscale Res. Lett.* **2017**, *12* (1), 377.
(41) Wang, J.; Li, J.; Zhao, N.; Sha, J.; Hao, S.; Liu, E.; Shi, C.; He, C.; Wang, D. {010}-Oriented Micro-Flower-like Hierarchical Bi_2WO_6 with High Adsorptivity and Visible-Light-Driven Photoactivity: Experimental Studies and First-Principles Modeling. *Appl. Surf. Sci.* **2015**, *324*, 698−704.
(42) Guo, M.; Zhou, Z.; Yan, S.; Zhou, P.; Miao, F.; Liang, S.; Wang, J.; Cui, X. Bi_2WO_6−BiOCl Heterostructure with Enhanced Photocatalytic Activity for Efficient Degradation of Oxytetracycline. *Sci. Rep.* **2020**, *10* (1), 18401.
(43) Li, H.; Zheng, Z.; Liu, M.; Jiang, H.; Hu, D.; Zhang, X.; Xia, L.; Geng, X.; Lu, J.; Cheng, X.; Wan, Y.; Yang, P. Visible Light Photo-treatment of Simulated Wastewater Activated by High-Efficient Photocatalyst: A Novel Heterojunction of Bi_2MoO_6 Balls and Pd Nanoskeletons. *Appl. Surf. Sci.* **2020**, *510*, No. 145468.
(44) Fang, X.; Rong, C.; Zhou, L.; Yin, C.; He, L.; Cui, H.; Lu, F.; Kuang, X. Enhanced Lithium Storage in Micrometer-Scale Tungsten Bronze $Mo_3Nb_2O_{14}$ by Molybdenum Reduction and Oxygen Deficiency. *Adv. Mater. Interfaces* **2021**, *8* (24), No. 2101016.
(45) An, W.; Wang, S.; Fu, Y.; Guan, Y.; Li, Z.; Xu, T.; Wang, H. Construction of Bi_2WO_6 with Oxygen Vacancies and Investigation on Mechanisms of Significantly Enhanced Photocatalytic Activity. *Desalination and Water Treatment* **2021**, *216*, 151−161.
(46) Lv, Y.; Yao, W.; Zong, R.; Zhu, Y. Fabrication of Wide−Range−Visible Photocatalyst Bi_2WO_{6-x} Nanoplates via Surface Oxygen Vacancies. *Sci. Rep.* **2016**, *6* (1), 19347.
(47) Hu, J.; Li, J.; Cui, J.; An, W.; Liu, L.; Liang, Y.; Cui, W. Surface Oxygen Vacancies Enriched FeOOH/Bi_2MoO_6 Photocatalysis-Fenton Synergy Degradation of Organic Pollutants. *Journal of Hazardous Materials* **2020**, *384*, No. 121399.
(48) Wei, Y.-Q.; Sun, C.; Chen, Q.-S.; Wang, M.-S.; Guo, G.-C. Significant Enhancement of Conductance of a Hybrid Layered Molybdate Semiconductor by Light or Heat. *Chem. Commun.* **2018**, *54* (100), 14077−14080.
(49) Kumar, A.; Navakoteswara Rao, V.; Kumar, A.; Venkatakrishnan Shankar, M.; Krishnan, V. Interplay Between Mesocrystals of $CaTiO_3$ and Edge Sulfur Atom Enriched MoS_2 on Reduced Graphene Oxide Nanosheets: Enhanced Photocatalytic

https://doi.org/10.1021/acsami.3c12563
ACS Appl. Mater. Interfaces XXXX, XXX, XXX−XXX

Performance under Sunlight Irradiation. *ChemPhotoChem.* **2020**, *4* (6), 427−444.
(50) Zhang, X.; Ren, G.; Zhang, C.; Xue, J.; Zhao, Q.; Li, R.; Wang, Y.; Fan, C. Assisting Bi_2MoO_6 Microspheres with Phenolic Resin-based ACSs as Attractive Tailor-Made Supporter for Highly-Efficient Photocatalytic CO_2 Reduction. *Green Energy & Environment* **2021**, *6* (5), 693−702.
(51) Li, H.; Yu, X.; Hao, X.; Zhang, Z.; Wang, Y.; Li, J. Preparation of Pt/γ-Bi_2MoO_6 Photocatalysts and Their Performance in α-Alkylation Reaction under Visible Light Irradiation. *Nanomaterials* **2020**, *10* (4), 646.
(52) Bai, J.; Li, Y.; Li, X.; Liu, L. Facile Preparation of 2D Bi_2MoO_6 Nanosheets−RGO Composites with Enhanced Photocatalytic Activity. *New J. Chem.* **2017**, *41* (15), 7783−7790.
(53) Zhang, Y.; Guo, L.; Wang, Y.; Wang, T.; Ma, T.; Zhang, Z.; Wang, D.; Xu, B.; Fu, F. In-situ Anion Exchange based Bi_2S_3/OV-Bi_2MoO_6 Heterostructure for Efficient Ammonia Production: A Synchronized Approach to Strengthen NRR and OER Reactions. *Journal of Materials Science & Technology* **2022**, *110*, 152−160.
(54) Chen, P.; Zhang, N.; Wang, S.; Zhou, T.; Tong, Y.; Ao, C.; Yan, W.; Zhang, L.; Chu, W.; Wu, C.; Xie, Y. Interfacial Engineering of Cobalt Sulfide/Graphene Hybrids for Highly Efficient Ammonia Electrosynthesis. *Proc. Natl. Acad. Sci. U. S. A.* **2019**, *116* (14), 6635−6640.
(55) Hao, Y.-C.; Guo, Y.; Chen, L.-W.; Shu, M.; Wang, X.-Y.; Bu, T.-A.; Gao, W.-Y.; Zhang, N.; Su, X.; Feng, X.; Zhou, J. W.; Wang, B.; Hu, C. W.; Yin, A. X.; Si, R.; Zhang, Y. W.; Yang, C. H. Promoting Nitrogen Electroreduction to Ammonia with Bismuth Nanocrystals and Potassium Cations in Water. *Nat. Catal.* **2019**, *2* (5), 448−456.
(56) Mohanty, S.; Sharma, M.; Kumar, A.; Krishnan, V. Hot Electron-Mediated Photocatalytic Degradation of Ciprofloxacin Using Au-Decorated $SrTiO_3$ and Ti_3C_2 MXene-Based Interfacial Heterostructure Nanoarchitectonics. *J. Phys. Chem. C* **2023**, *127* (36), 17711−17722.
(57) Kumar, A.; Kumar, M.; Rao, V. N.; Shankar, M. V.; Bhattacharya, S.; Krishnan, V. Unraveling the Structural and Morphological Stability of Oxygen Vacancy Engineered Leaf-Templated $CaTiO_3$ towards Photocatalytic H_2 Evolution and N_2 Fixation Reactions. *J. Mater. Chem. A* **2021**, *9* (31), 17006−17018.
(58) Zhang, Y.; Liu, X.; Sun, H.; Zhang, J.; Gao, X.; Yang, C.; Li, Q.; Jiang, H.; Wang, J.; Xu, D. Strong Self-Trapped Exciton Emissions in Two-Dimensional Na-In Halide Perovskites Triggered by Antimony Doping. *Angew. Chem., Int. Ed.* **2021**, *60* (14), 7587−7592.

https://doi.org/10.1021/acsami.3c12563
ACS Appl. Mater. Interfaces XXXX, XXX, XXX−XXX